EDGE ARTICLE

Check for updates

An excitation-wavelength-dependent organic photoluminescent molecule with high quantum yield integrating both ESIPT and PCET mechanisms†

Mengyuan Song,‡[ad] Meng Liu,‡[b] Xue Zhang, [c] Haijuan Qin,[e] Jinglu Sun,[fd] Juanjuan Wang,*[d] Qian Peng,[d] Zhiwei Zhao, [g] Guohui Zhao,[b] Xianchang Yan,[bd] Yongxin Chang, [a] Yahui Zhang, [a] Dongdong Wang,[a] Junhui Wang, *[bd] Jianzhang Zhao *[c] and Guangyan Qing *[ad]

Excitation wavelength-dependent (Ex-De) chromophores, which exhibit changes in spectral composition with varying excitation wavelengths, have garnered significant interest. However, the pursuit of novel photoluminescence (PL) mechanisms and high luminescence quantum yields is facing huge challenges. Here, we discover that the introduction of a spinacine moiety to 2-(2-hydroxy-5-methylphenyl) benzothiazole, a traditional excited-state intramolecular proton transfer (ESIPT) fluorophore, results in a novel Ex-De PL molecule. The luminescent color of this compound can be effectively modulated from greenish-blue to yellow-green by adjusting either the excitation wavelength or temperature. Transient absorption and spectroelectrochemistry spectra elucidate the underlying mechanism, demonstrating the roles of ESIPT and proton-coupled electron transfer (PCET). When embedded in a poly(vinyl alcohol) film, the composite exhibits remarkable Ex-De PL behavior, achieving absolute fluorescence quantum yields of 55.6% (λ_{ex}: 396 nm) and 69.6% (λ_{ex}: 363 nm), as well as phosphorescence at room temperature. These properties highlight its potential for multiple encryption features, enhancing its application in anti-counterfeiting technologies.

Introduction

Excitation-wavelength-dependent (Ex-De) luminophores have recently attracted significant interest due to their photoluminescence (PL) properties, including emission wavelength, band shape, lifetime, and quantum yield, all of which are believed to be influenced by the excitation wavelength (λ_{ex}).[1,2] These materials have a wide range of potential applications in sensing,[3,4] cellular imaging,[5] anti-counterfeiting technologies,[6] single molecule white light emitters,[7,8] and various optoelectronic devices.[9,10] However, this luminescent behavior has primarily been observed in nanoparticles,[11] such as carbon[12]/silica dots, and metal complexes,[13] including [Au(NHC)$_2$][M(CN)$_2$][14] and [Pt(tpp)(ed)]$^+$[Pt(ftpp)(CN)$_2$].[15] In nanoparticles, modifications such as size adjustments, element doping, and changes in surface functional groups can introduce new energy-level structures for electronic transitions. In metal complexes, metallophilic interactions among d^6, d^8 and d^{10} transition metal complexes can bestow tunable luminescence properties,[16,17] with the distance between metal ions significantly influencing the characteristics of the Ex-De luminophores. Although these methods offer promising solutions, they often encounter drawbacks such as high biotoxicity, complex preparation requirements, limited metal ion resources, and phase segregation, which hinder the advancement of the field.[18,19] An ideal approach would involve the development of small organic molecules capable of exhibiting Ex-De multiple

[a]State Key Laboratory of Medical Proteomics, National Chromatographic R. & A. Center, CAS Key Laboratory of Separation Science for Analytical Chemistry, Dalian Institute of Chemical Physics, Chinese Academy of Sciences, Dalian 116023, P. R. China. E-mail: qinggy@dicp.ac.cn

[b]State Key Laboratory of Molecular Reaction Dynamics, Dalian Institute of Chemical Physics, Chinese Academy of Sciences, Dalian 116023, P. R. China. E-mail: wjh@dicp.ac.cn

[c]State Key Laboratory of Fine Chemicals, Frontiers Science Centre for Smart Materials, School of Chemical Engineering, Dalian University of Technology, Dalian 116024, P. R. China. E-mail: zhaojzh@dlut.edu.cn

[d]University of Chinese Academy of Sciences, Beijing 100049, P. R. China. E-mail: jjwang@ucas.ac.cn

[e]Research Centre of Modern Analytical Technology, Tianjin University of Science and Technology, Tianjin 300457, P. R. China

[f]Key Laboratory of Chemical Lasers, Dalian Institute of Chemical Physics, Chinese Academy of Sciences, Dalian 116023, P. R. China

[g]Laboratory of Advanced Spectroelectrochemistry and Li-ion Batteries, Dalian Institute of Chemical Physics, Chinese Academy of Sciences, Dalian 116023, P. R. China

† Electronic supplementary information (ESI) available. See DOI: https://doi.org/10.1039/d4sc08197h

‡ These authors contributed equally.

emissions. However, this remains challenging due to the PL behavior of most fluorescent molecules, which typically follows Kasha's rule.[20–22] According to this rule, emission occurs only from the lowest excited state of a given (singlet or triplet) multiplicity, thus making it independent of excitation energy.

Considerable efforts have been dedicated to achieving Ex-De PL in pure organic materials.[2] According to Jablonski's energy level diagram, methods for achieving Ex-De PL include: (1) constructing multiple luminescent triplet states using materials such as amorphous organic materials doped[23] or bonded[24] with polymers, non-conjugate clusters[19,25] and tris(4-chlorophenyl) phosphine oxide (CPO),[26] and (2) creating a large energy gap in the excited state to inhibit internal conversion processes and promote high-energy state luminescence.[27,28] In 2023, Zhang *et al.* summarized the current state of Ex-De materials in a review article,[29] highlighting that the presence of multiple excited states is a prerequisite for this phenomenon. They also pointed out that controlling single-chromophore-based Ex-De chromophores across multiple excited states remains in the early stages of development. Additionally, existing Ex-De molecules often exhibit limited luminescence capabilities, which restricts their broader application. This limitation could be attributed to two primary reasons: first, organic molecules typically exhibit low singlet state photoluminescence quantum yields (PLQY), because the rates of various non-radiative transitions often out-compete those of the radiative transitions, significantly influenced by intersystem crossing (ISC).[25,30] Second, achieving consistent brightness is challenging.[26] In organic molecules exhibiting dual-emission Ex-De luminescence, there is often a notable difference in the PLQY between the two emission wavelengths. A report by Wu suggests that the linear correlation between the S_n–S_1 energy gap and the PLQY ratios of S_n emission results in a notably lower PLQY from the S_n state compared to that from the S_1 state.[27] These challenges must be addressed to facilitate the practical applications of Ex-De materials in anti-counterfeiting, information storage, biosensing, and multicolor displays. It is essential to enhance overall PLQY, particularly by improving the luminescence intensity and quantum yield of the weakly emitting electronic state in the material.[31]

Here we report a novel molecular system designed to overcome the limitations of existing approaches. This work builds upon 2-(2-hydroxyphenyl)-benzothiazole (HBT), a well-known organic compound recognized for its characteristic excited-state intramolecular proton transfer (ESIPT) behavior.[32–34] We introduce a spinacine moiety at the *ortho* position of the phenolic group of HBT, generating a new compound designated as **2** (Fig. 1a). Interestingly, **2** exhibits distinct photophysical behavior compared to its parent compound **1** in methanol (CH$_3$OH), including temperature-dependent changes in emission wavelength, the emergence of new fluorescent emission under 400 nm excitation, the appearance of an Ex-De phenomenon, and phosphorescence. Femtosecond (fs) and nanosecond (ns) transient absorption (TA) spectra clearly demonstrate that the introduction of the spinacine moiety markedly promotes the ESIPT process as the temperature decreases from 300 K to 180 K, resulting in a stronger

fluorescence switch under 340 nm excitation. In contrast, **2** displays distinct PL behaviors when excited at 400 nm. Spectroelectrochemistry analysis indicates that the PCET process dominates the luminescence mechanism of **2**.

The PL switching between ESIPT and PCET, triggered by varying the λ_{ex} leads to a remarkable Ex-De phenomenon, which has rarely been reported previously. It is important to note that the PCET process is crucial for enhancing the efficiency of redox reactions and controlling reaction selectivity. This mechanism plays a vital role in biological energy conversion and enzyme-catalyzed reactions, while also optimizing the performance of energy materials in materials science.[35] This study represents the first demonstration of PCET in the Ex-De system, thereby advancing our understanding of molecular design. Additionally, this effect persists when **2** is transferred from the CH$_3$OH solution to a poly(vinyl alcohol) (PVA) film. The resulting **2**-PVA composite film not only displays a pronounced Ex-De effect but also exhibits brightness-variable luminous colors, with PLQY values reaching 55.6% (λ_{ex}: 396 nm) and 69.6% (λ_{ex}: 363 nm), both of which are substantially higher than those of previously reported Ex-De organic molecules. Finally, we illustrate a proof-of-concept for anti-counterfeiting applications, demonstrating the potential utility of this system. This design strategy could be expanded to other derivatives (**3–6**), inspiring the development of creative and highly efficient Ex-De systems in the future.

Results and discussion

Remarkable differences between 1 and 2 in the photophysical properties

First, compound **2** was analysed using high-performance liquid chromatography (HPLC) with a C18 reversed-phase column (Fig. S1†). The single peak observed at a retention time of 14 min indicated that **2** was pure, confirming that the subsequent observations were not due to impurities. As shown in Fig. 1b, the absorption spectra of **2** in CH$_3$OH solution displays two distinct absorption bands centered at 298 nm and 341 nm, which closely resemble those of the parent molecule **1**. We further investigated the PL spectra of these two luminophores in CH$_3$OH and dichloromethane (CH$_2$Cl$_2$), respectively. As anticipated, upon 360 nm excitation in the aprotic solvent CH$_2$Cl$_2$ (Fig. 1c), both **1** and **2** exhibit the maximum emission wavelength at 532 nm. Identical excitation spectra were also observed for these two compounds, which indicated that **2** inherited the fundamental characteristics of **1** and could undergo an efficient ESIPT process. In contrast, when excited at 347 nm in the protic solvent CH$_3$OH, **2** emits greenish-blue light with a PL peak at 472 nm, which represents an 83 nm red-shift compared to that of **1** (Fig. 1d). Furthermore, the excitation peak of **2** also experiences a 20 nm red shift compared to that of **1**, along with the appearance of a new shoulder peak at 390 nm. These remarkable differences in the emission and excitation spectra indicated that **1** and **2** possess distinct photophysical properties in CH$_3$OH.

The literature has extensively documented that temperature significantly influences the PL properties of a substance.[36,37] To investigate this relationship, a temperature-dependent
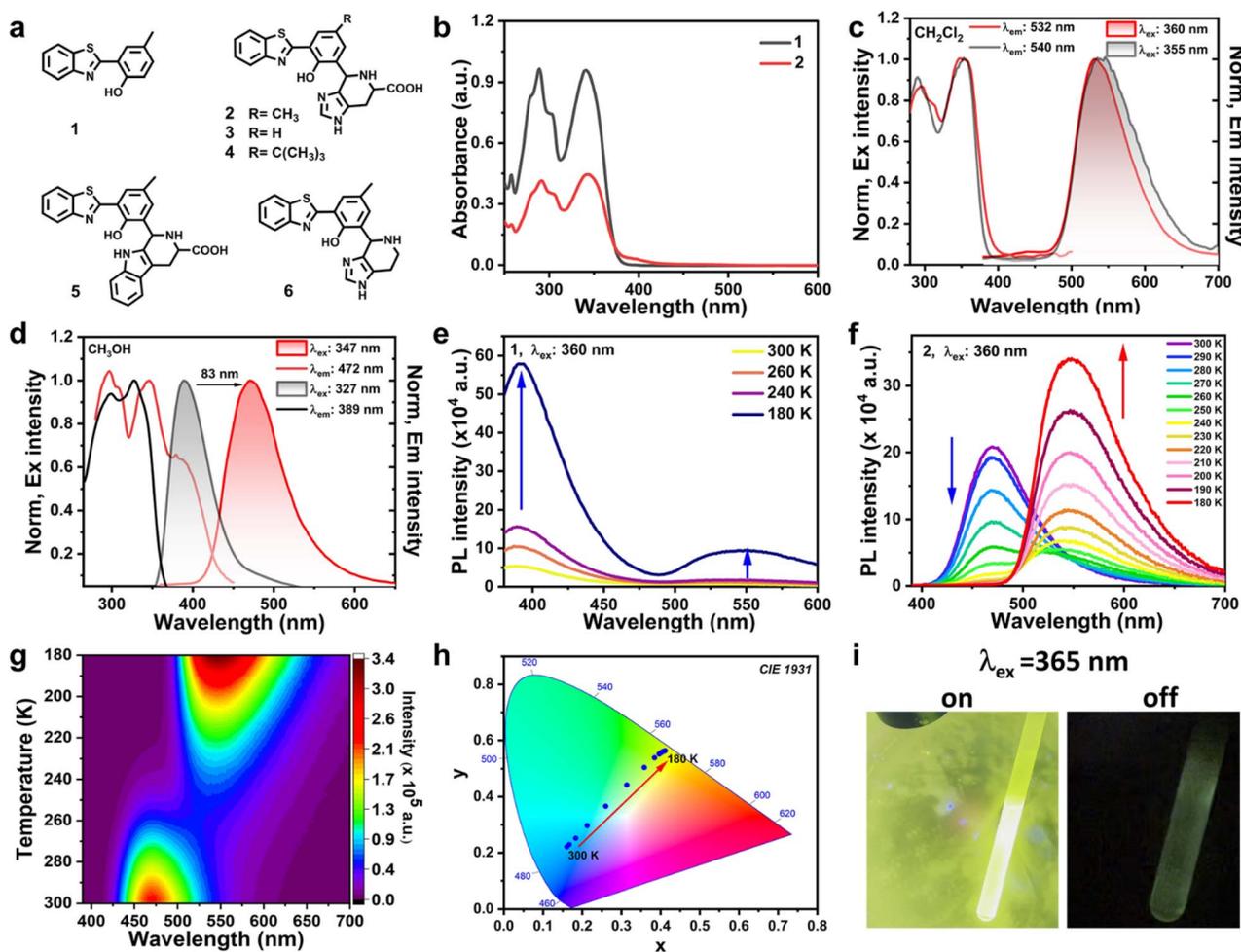
Fig. 1 (a) Molecular structures of 1–6. (b) UV-vis absorption spectra of 1 (black) and 2 (red) in CH_3OH at a concentration of 50 µM. The inset shows an enlarged view between 370 nm and 450 nm. (c and d) Normalized excitation (solid lines) and emission spectra (gradient fill) of 1 (black) and 2 (red) in CH_2Cl_2 (c) and CH_3OH (d), respectively. (e and f) Temperature-dependent PL spectra of 1 (e) and 2 (f) in CH_3OH solution, λ_{ex}: 360 nm. (g) Corresponding temperature-emission mapping of 2. (h) Commission International de l' Éclairage (CIE) chromaticity coordinates for the temperature-dependent emission (temperature range: 300–180 K). (i) Photographs of 2 under LED irradiation at 365 nm (left) and after cessation of light irradiation (right). Concentrations: 33.3 µM.

fluorescence test was conducted. As shown in Fig. 1e, under 360 nm excitation, the maximum PL peak of 1 remained at 390 nm when the temperature decreased from 300 K to 180 K. Additionally, the PL intensity gradually increased at lower temperatures. At 180 K, which is close to the freezing point of CH_3OH, the luminescence intensity at 390 nm sharply increased, accompanied by the emergence of a new emission peak at 545 nm, corresponding to the keto-form structure of 1.[34] In general, as temperatures decrease, molecular rotation and vibration are inhibited, restricting non-radiative transitions and leading to enhanced fluorescence efficiency and intensity.[38]

Interestingly, 2 exhibits distinctly different PL behavior in response to temperature changes. As shown in Fig. 1f, when the temperature is decreased from 300 K to 180 K, the characteristic emission peak of 2 at 472 nm gradually decreases and completely disappears below 240 K. Concurrently, a new PL peak emerges at 545 nm at 250 K, with its intensity increasing gradually as the temperature decreases to 180 K. A two-

dimensional (2D) contour map (Fig. 1g) further illustrates this temperature-dependent change in emission wavelength, showing two distinct emission centers under the same λ_{ex} of 360 nm. The transition between the PL peak at 472 nm and that at 545 nm resulted in a notable PL color change from greenish-blue ($(x, y) = (0.16, 0.22)$) to yellowish-green ($(x, y) = (0.41, 0.56)$) as the temperature decreased, as displayed in the corresponding CIE diagram (Fig. 1h).

Furthermore, an NMR tube containing a CH_3OH solution of 2 was placed in liquid nitrogen and irradiated with a UV flashlight as the excitation light source. Upon illumination, 2 emitted yellow light. Notably, after the light was turned off, delayed yellow luminescence remained visible to the naked eye (Fig. 1i).

Ex-De behaviors of 2

The observed phenomena motivated our interest to investigate the photophysical properties of 2 in CH_3OH. Excitation-

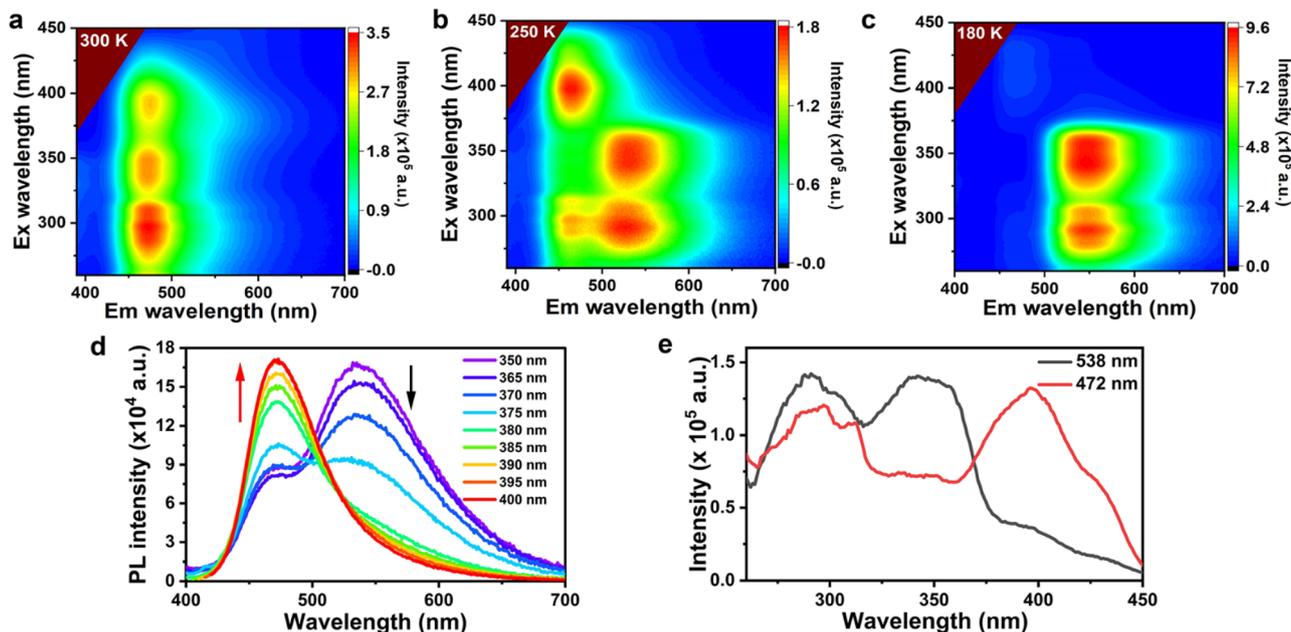Fig. 2 Excitation–fluorescence mapping of **2** in CH_3OH at (a) 300 K, (b) 250 K, and (c) 180 K, with a concentration of 33.3 μM. (d) PL spectra of **2** in CH_3OH at 250 K with an λ_{ex} range of 350–400 nm. (e) Excitation spectra of **2** in CH_3OH at 250 K, emission wavelength: 472 nm (red) and 538 nm (black).

emission mappings were measured at 300 K, 250 K, and 180 K, respectively (Fig. 2a–c). PL spectra at other temperatures are included in the ESI (Fig. S2†). At 300 K, when λ_{ex} varied from 260 nm to 450 nm, the PL peak consistently appears at 472 nm (Fig. 2a). When the temperature decreased to 250 K, two distinct PL peaks become evident in the 2D contour plots (Fig. 2b). The first set of emission peaks, located at 538 nm, could be excited by λ_{ex} in the range of 280 nm to 360 nm, while the second set of emission peaks at 473 nm was excited by λ_{ex} in the range of 380 nm to 440 nm. When the temperature was further decreased to 180 K, the PL peak of **2** was solely found at 545 nm with λ_{ex} in the range of 250 nm to 380 nm (Fig. 2c), while no evident PL peak is detected at λ_{ex} beyond 380 nm. This behavior illustrated a desirable Ex-De PL color-switching process, with the luminescence color transitioning from yellowish-green ((x, y) = (0.32, 0.45)) to greenish-blue ((x, y) = (0.17, 0.24)) in response to changes in λ_{ex}, as displayed in the corresponding CIE diagram (Fig. S3 and Table S1†).

The PL spectra of **2** under different λ_{ex} (Fig. 2d) further confirm the Ex-De PL behavior at 250 K. As λ_{ex} increases from 350 nm to 400 nm, the PL intensity at 538 nm decreases remarkably. Conversely, the PL intensity at 472 nm begins to increase when λ_{ex} exceeds 375 nm, reaching an optimal value at 400 nm. The excitation spectra (Fig. 2e) further illustrate the direct relationship between the excitation and emission wavelengths. The excitation peak near 350 nm contributes to the emission at 538 nm (the black line in Fig. 2e). In sharp contrast, the excitation peak at 400 nm corresponds to the emission at 472 nm (red line in Fig. 2e). These observations demonstrated the characteristic Ex-De PL behavior of **2**. These observations demonstrated the characteristic Ex-De PL behaviours of **2**.

Under the same conditions, compound **1** did not exhibit Ex-De PL behaviour. Its excitation dependent emission spectra (Fig. S4†) revealed that the emission peak was consistently located at 390 nm, unaffected by variations in λ_{ex} or temperature. This highlighted the significant role of spinacine in **2** regarding the observed Ex-De PL behaviour.

Photoluminescence mechanism under 340 nm excitation

2 exhibits distinct PL peaks when irradiated with light at 340 nm and 400 nm. To elucidate the potential PL mechanisms, we performed a series of analyses, including control experiments and femtosecond transient absorption (fs-TA) and nanosecond transient absorption (ns-TA) measurements. Initially, we focused on the PL mechanism with λ_{ex} set at 340 nm.

To investigate the evolution of the excited states in **1** and **2** excitation with a femtosecond pulse at 340 nm, we recorded fs-TA spectra using a custom-built measurement system (Fig. S5†).[39] This technique, which utilizes ultrafast laser pump-probe technology, enables the examination of photophysical processes in molecules following excitation. The fs-TA spectra provide essential information, including ground state bleaching (GSB), excited state absorption (ESA), and stimulated emission (SE), offering valuable insights into the relaxation processes of excited states. Fig. 3a shows the 2D contour plots of the fs-TA spectra for **2** in CH_3OH following 340 nm excitation, which displays similar spectra to **1** (Fig. S6†). The detection wavelength is presented on the abscissa, while the delay time post-excitation is on the ordinate, with absorbance changes (ΔA) represented by color coding. The major spectral features include two positive absorption bands: Band A (peaking at 408
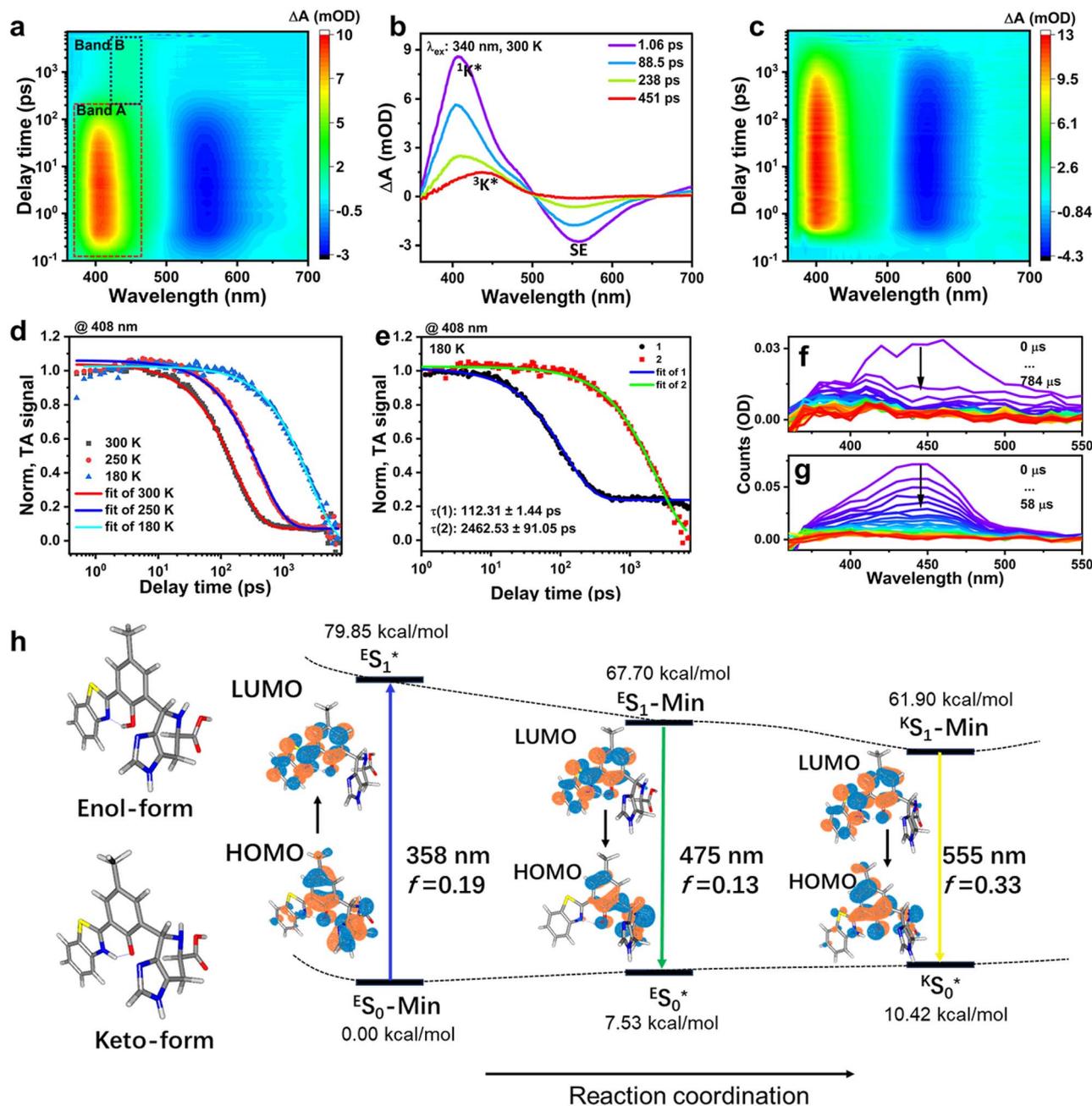
Fig. 3 PL mechanism study of 2 upon 340 nm excitation (a) the 2D contour plots of fs-TA spectra for 2, excited by 340 nm light (0.33 mM), recorded using a custom measurement system at DICP, CAS (ESI Fig. 4†), at a temperature of 300 K. (b) fs-TA spectra of 2 at 1.06 ps (purple), 88.5 ps (blue), 238 ps (green), and 451 ps (red). (c) 2D contour plots of the fs-TA spectra of 2 at 180 K. (d) A comparison of fs-TA kinetic traces of 2 (at 408 nm) at 300 K (black), 250 K (red), and 180 K (blue), with solid lines representing the corresponding monoexponential fitting. (e) Comparison of fs-TA kinetic traces for 1 (black) and 2 (red) at 180 K, with solid lines showing monoexponential fitting. (f and g) ns-TA spectra of 2 (f) and 1 (g) at various delay times after excitation by 355 nm, recorded using an LP980 laser flash photolysis spectrometer (Edinburgh Instruments, UK). TA signals (i.e., absorbance change, ΔA) are displayed in the unit of optical density (OD). (h) Theoretical analysis of ESIPT in 2. The Gibbs free energy surface together with the structures of the enol and keto isomers, the frontier molecular orbitals (HOMO (Highest Occupied Molecular Orbital) and LUMO (Lowest Unoccupied Molecular Orbital)), relative energies and photophysical properties (absorption/emission wavelengths and oscillator strengths (f)) were calculated at the TD-DFT/B3LYP/6-31G*/PCM(CH$_3$OH) level.

nm) and Band B (peaking at 450 nm), which develop in sequence and gradually attenuate over time. The ESA Band A corresponds to a broad SE band centered at 589 nm. The characteristic spectra are illustrated in Fig. 3b. According to

previous reports, the photo-isomerization from the enol-excited state (E*) form to the keto-excited state (K*) form occurs extremely rapidly.[40,41] Consequently, at the beginning, the ESA band A at 408 nm of the K* singlet state (^{1}K*) and its

corresponding SE features in the range of 500–650 nm dominate the spectra. The ESA and SE features decay within dozens of picoseconds, accompanied by the emergence of a new absorption feature at 450 nm, which could be reasonably attributed to the triplet state ($^3K^*$) of the keto-form due to its intrinsic ISC, as supported by the findings of Aly, S. M. and co-workers (Fig. 3b).[42] The global fitting of the evolution kinetics for the $^1K^*$, and $^3K^*$ features is presented in Fig. S7a.† According to the fit, the average decay time constant of $^1K^*$ is 160 ps at 300 K. The 2D contour plots of the fs-TA spectra of **2** at 180 K are depicted in Fig. 3c. The characteristic ESA band of $^1K^*$ of **2** exhibits a stronger signal and a longer delay time compared to observations at 300 K (Fig. 3a). Simultaneously, the SE_{K*}^1 band shows consistent variations.

We further compared the fs-TA kinetic traces of **2** (monitored at 408 nm) at different temperatures (Fig. 3d and Table S2†). The decay time at 180 K is significantly longer than that at 250 K or 300 K. A single exponential is used to fit the data at different temperatures (Table S3†). As the temperature decreased from 300 K to 180 K, the lifetime τ value increased from 164.0 ± 2.5 ps to 2462.5 ± 91.1 ps, which indicated that the lower temperature was favorable for the stability of $^1K^*$, thus promoting the ESIPT process and contributing to the strong luminescence at 550 nm. This is consistent with the global fit data (Fig. S7†). Further, as illustrated in Fig. S8† and 3e, **2** exhibits a longer evolution time than **1** at both 300 K and 180 K, with correspondingly larger τ values. This indicates that the addition of ligands to molecule **2** is beneficial to the formation of intramolecular hydrogen bonds, promoting the ESIPT process.[43,44]

In addition, the $^1K^*$ species of **1** and **2** could undergo ISC to the $^3K^*$, which was also observed in the ns-TA spectra measurements (Fig. 3f, g, S9 and S10†). The $^3K^*$ species of **2** displayed a shorter lifetime (6.5 μs) than that of **1** (11.24 μs). All the above results suggested that the introduction of the spinacine unit inhibited the non-radiative transition of the $^1K^*$ excited state and the ISC process from $^1K^*$ to $^3K^*$.

Time-dependent density functional theory (TD-DFT) calculations were performed at the B3LYP/6-31G*/PCM(CH$_3$OH) level to simulate the ESIPT process of **2**, revealing distinct photophysical properties between the enol and keto tautomer.

As shown in Fig. 3h, upon 358 nm excitation, the enol-form is initially promoted to the singlet excited state ($^ES_1^*$) and subsequently relaxes to the energy minimum of the $^ES_1$ state ($^ES_1$-Min), emitting fluorescence at 475 nm. Electron density analysis indicates that the $^ES_1$ state originates from an intramolecular charge transfer (CT) from the phenolic ligand to the HBT moiety, corresponding to a hybrid local excitation (LE) and charge transfer (CT) character. In addition to radiative decay, the $^ES_1$-Min can undergo isomerization to the keto tautomer along a barrierless energy pathway, reaching the minimum of the $^KS_1$ state ($^KS_1$-Min). This results in a red-shifted emission at 555 nm, with a higher oscillator strength ($f = 0.33$) compared to the 475 nm emission ($f = 0.13$), consistent with the experimental steady-state spectrum. The $^KS_1$ state primarily exhibits LE feature localized on the HBT moiety (Fig. 3h) and is thermodynamically more stable than the $^ES_1$ state (enol: 67.70 kcal mol; keto: 61.90 kcal mol^{-1}). These findings confirm that

the keto tautomer is the dominant species in the photoluminescence of the ESIPT process, which is in agreement with the experimental observations. Under cryogenic conditions, the substantial suppression of thermal fluctuations restricts molecules predominantly to their lowest vibrational states ($v = 0$ or $v = 1$). This effectively minimizes non-radiative decay pathways, leading to a marked improvement in radiative efficiency—a phenomenon consistent with the experimentally observed enhancement of the keto-form luminescence at low temperatures.

PL mechanism under 400 nm excitation

Using identical methods, we investigated the excited state transitions of the compounds under 400 nm excitation. Compound **1** does not exhibit PL under excitation at 400 nm, due to its lack of absorption in the 380 nm to 500 nm range. To explore the excited-state dynamics of **2** at 300 K, fs-TA spectra were utilized. As shown in Fig. 4a, the 2D contour plots of the fs-TA spectra of **2** reveal an ESA peak at 420 nm, which gradually increases in intensity and begins to decay after 225 ps. This decay is accompanied by a blue shift in the corresponding SE peak from 580 nm to 500 nm. Fig. 4b further displays the evolution of these features in the fs-TA spectra captured at 956 fs and 4.1 ns after excitation. In addition, when **2** is excited at 420 nm, the ns-TA spectra reveal a band at 500 nm, which could be fitted with a monoexponential function characterized by a τ of 11.61 μs (inset of Fig. 4b and S11†). Notably, the maximum emission wavelength of this long-lived species (500 nm) was different from that observed in the ns-TA spectra of **2** (450 nm) upon 340 nm excitation. We compared the fs-TA kinetic traces of **2**, monitored at 424 nm, upon λ_{ex} of 400 nm and 340 nm at 300 K. As depicted in Fig. 4c, excitation at 340 nm results in the rapid formation of the excited species ($^1K^*$) of **2**, followed by a gradual decay starting at 2.7 ps. In sharp contrast, excitation at 400 nm leads to a slower formation of the excited species of **2**, with decay commencing after 200 ps. These findings clearly indicated that the excited species generated under 400 nm excitation differed from that produced upon 340 nm excitation.

Subsequently, we acquired the 2D contour plots of the fs-TA spectra of **2** under 400 nm excitation at 180 K (Fig. S12a†). Compared to the observations at 300 K (Fig. 4a), the decay process and lifetime of the excited species remain similar. However, the corresponding SE peak gradually increases in intensity while undergoing a red shift from 473 nm to 494 nm. This trend was further supported by the fs-TA spectra at 997 fs and 2.5 ns (Fig. S12b†) recorded at 180 K, which differ from those observed at 300 K. Notably, at 180 K, the 2D color plots of the TA spectra of **2** under 400 nm excitation (Fig. S12a†) exhibit distinct features compared to those under 340 nm excitation (Fig. 3c).

To investigate the origin of the ESA signal, compound **1** was introduced to conduct TA spectrum measurements. However, due to its lack of absorption in the 380 nm to 500 nm range, the TA signals of **1** could not be collected under excitation at 400 nm. Furthermore, **1** was allowed to dissolve in NaOH$_{(aq)}$/CH$_3$OH solution, its anionic form displays a similar positive
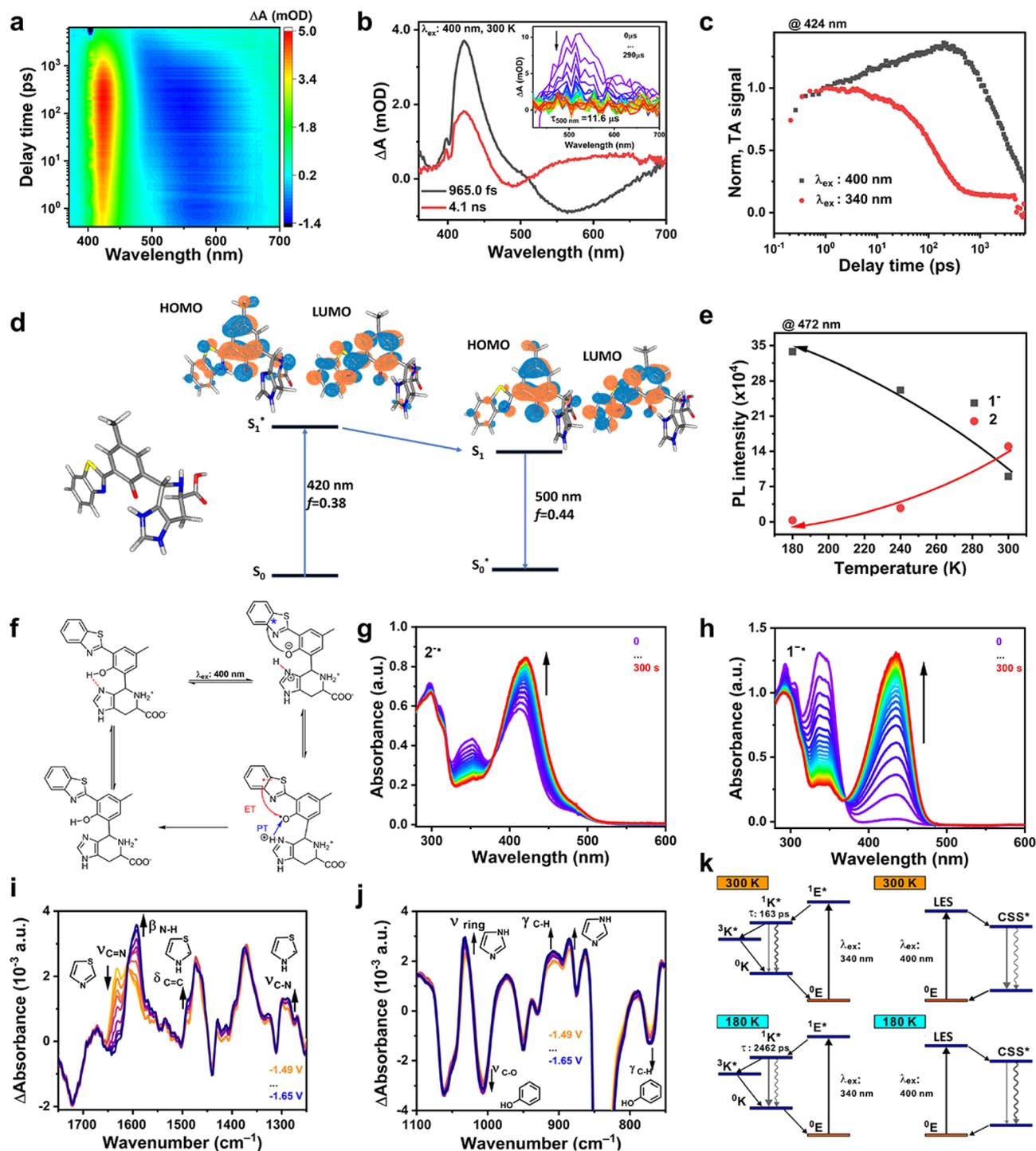
Fig. 4 PL mechanism study of **2** upon 400 nm excitation. (a) The 2D contour plots of fs-TA spectra of **2** excited by 400 nm light at 300 K and the corresponding fs-TA spectra (b) of **2** at 965 fs (black) and 4.09 ns (red). The inset in (b) shows the ns-TA spectra of **2** in deaerated CH$_3$OH, λ_{ex}: 420 nm. (c) Comparison of fs-TA kinetic traces of **2** (at 424 nm) excited by 400 nm (black) and 340 nm (red) light at 300 K. (d) Theoretical analysis of the absorption and emission processes of **2**, where the proton from HBT is transferred to the imidazole group. The frontier molecular orbitals of HOMO, LUMO, absorption/emission wavelengths and corresponding f were evaluated at the TD-DFT/B3LYP/6-31G*/PCM(CH$_3$OH) level. (e) Temperature-dependent emission profiles at 472 nm for the anion of **1** (black) and **2** (red) following 400 nm excitation. (f) A schematic of photochemical e$^-$/H$^+$ charge separation and charge recombination in **2**. (g and h) Evolution of UV-vis absorption spectra of **2** (g) and **1** (h) under applied reduction voltages of −1.60 V and −1.55 V, respectively, at a concentration of 1.0 mM; Ag/AgNO$_3$ was used as the reference electrode. The spectra were recorded *in situ* using a spectroelectrochemical cell (1 mm optical path) in deaerated DMSO. (i and j) *In situ* FT-IR spectra of **2** (40 mM) on a glassy-carbon (GC) electrode with external reflection configuration, recorded in the 1750−1300 cm^{-1} region (i) and the 1100−750 cm^{-1} region (j). Solvent: DMSO, 0.1 M [Bu$_4$N]PF$_6$, reference electrode: Ag. (k). Jablonski diagram of the possible photophysical processes for the PL.

ESA signal in 420 nm (Fig. S13†).[45] Fluorescence lifetime measurements of the anionic species of **1** in 5% TEA/CH$_3$OH solution revealed a striking similarity to the lifetime of **2** at 472 nm in CH$_3$OH (Fig. S14†). This evidence suggests that the species generated upon 400 nm excitation of **2** in CH$_3$OH originates from the deprotonated conformation of the HBT group. Further computational studies demonstrate that in the conformation of **2**, the proton resides on the imidazole group, forming an imidazolium cation, while the phenol group loses a proton to yield the HBT's anion, exhibiting an absorption band at 420 nm ($f = 0.38$) and corresponding emission at 500 nm ($f = 0.44$), which align well with experimental observations (Fig. 4d).

Surprisingly, variable-temperature fluorescence spectra of **1** in 5% TEA/CH$_3$OH solution show that the anionic emission intensity gradually increases as the temperature decreases—a trend opposite to that observed for **2** (Fig. 4e and S15†). This indicates that the formation of the HBT's anion in **2** is driven not by solvent–solute interactions but by intramolecular hydrogen bonding.[46] The spinacine ligand, with its imidazole moiety, forms a significantly stronger hydrogen bond with the phenol group than methanol–phenol. Consequently, when the anionic form of HBT is photoexcited, it generates a locally excited state (LES), and the protonated ligand may open new relaxation pathways.

We proposed that the proton-coupled electron transfer (PCET) process might take place upon excitation at 400 nm (Fig. 4f).[47] In the excited state, compound **2** undergoes a transition from a LES to a charge-separated state (CSS), accompanied by simultaneous proton transfer (PT) and electron transfer (ET). Ultimately, the light energy is converted into chemical bond energy. This process potentially generates cationic and anionic radical intermediates.[48] Using spectroelectrochemistry (Fig. S16†), we further characterized the absorption bands of the radical anion (Fig. 4g and h) and radical cation (Fig. S17 and S18†).[49–51] When a reduction potential of −1.60 V (*vs.* Ag/AgNO$_3$) was applied to **2**, the absorption intensity of the band at 422 nm gradually increases from 0.54 to 0.84 over time (Fig. 4g), which could be attributed to the formation of the electrochemically generated radical anion **2**$^{-•}$. Meanwhile, when a reduction potential of −1.55 V (*vs.* Ag/AgNO$_3$) was applied to **1**, a new absorption band centered at 430 nm emerged (Fig. 4h) and increased markedly from 0 to 1.3 over time, suggesting the formation of the electrochemically generated radical anion **1**$^{-•}$. This indicated that the anionic radical of **2** originated from its parent structure, compound **1**. Moreover, the new absorption band at 430 nm was consistent with the positive signal observed in the fs-TA spectrum of **2**. In other words, after **2** is excited by 400 nm light, charge separation occurs in the excited state, leading to the generation of a radical anion originating from **1**. Furthermore, when an oxidation potential of 0.27 V (*vs.* Ag/AgNO$_2$) was applied to **2**, the absorption intensity of the band at 422 nm gradually decreased from 0.46 to 0.11 over time (Fig. S17†). In contrast, under the same conditions, no credible changes in the UV-vis spectra (Fig. S18†) were detected when the positive potential was applied to **1**. These control experiments

indicated that **1** primarily functioned as an electron acceptor, while the spinacine unit in **2** acted as an electron donor.

To reveal the excitation characteristics of the electrons within the system, we intended to use hole–electron analysis, an intuitive and versatile method.[52,53] Fig. S19† shows the contour map of the hole and electron distributions corresponding to their maximum absorption of **2**, where the green area represents the electron distribution and the blue area indicates the hole distribution. Notably, distinct hole and electron distributions are observed in the imidazole, phenol, and benzothiazole regions. These different distributions indicate that the direction of excited-state electron transfer is from the imidazole moiety to the parent structure (Table S3 and Fig. S20†). Moreover, once the charge separation occurs, the negative charge on the parent structure is more conducive to coupling with protons. Therefore, it is conducive for the proton on the imidazole to return to the parent structure.

In situ Fourier transform infrared spectroscopy (FT-IR) is effective for identifying specific bonding changes resulting from protonation and deprotonation during a PCET process (Fig. S21†).[54,55] Fig. 4i shows the IR spectra of **2** at a potential of 1.49–1.65 V (*vs.* Ag) in the region of 1750–1250 cm^{-1}. At this reduction potential, the parent structure of **2** accepts electrons, facilitating proton transfer, with the N atom of the benzothiazole structure acting as a proton acceptor to generate benzothiazole free radicals and phenolic anions. During this process, the C=N bond is transformed into a C–NH bond. The changes observed in the infrared spectra at 1288, 1490, 1590, and 1631 cm^{-1} indicated the occurrence of the PCET process. The peak at 1590 cm^{-1} is attributed to the N–H in-plane bending vibration of the benzothiazole moiety, while the peak at 1631 cm^{-1} is attributed to C=N stretching within the benzothiazole. The peaks at 1490 and 1288 cm^{-1} represent the deformation vibration of C=C and the stretching vibration of C–N, respectively. Notably, as the intensity of the peak at 1631 cm^{-1} decreases, the intensity of the peak at 1590 cm^{-1} increases. Additionally, the intensities of the peaks at 1490 and 1288 cm^{-1} also show a continuous increase.

In addition, imidazole, being a basic group, may form hydrogen bonds with a hydroxyl group on phenol under non-photoexcited conditions. However, at the reducing voltage, benzothiazole accepts electrons to form radicals, which increases its alkalinity and promotes the transfer of protons to benzothiazole. This leads to the conversion of imidazole from a positively charged state to a neutral state.[56] As shown in Fig. 4j, the peaks at 1031, 908, and 885 cm^{-1} correspond to symmetric stretching vibration and out-of-plane bending vibration of C–H bonds in the imidazole group, with their peak intensities increasing continuously within the reduction voltage of 1.49–1.65 V (*vs.* Ag). Additionally, the intensities of both the C–O stretching band at 1006 cm^{-1} (deprotonated phenolate) and the benzene ring C–H out-of-plane bending at 771 cm^{-1} decrease. These reductions directly reflect the phenolic deprotonation, which subsequently induces electron density redistribution in the aromatic system. These spectral changes of the IR bands provide favorable evidence for the occurrence of the PCET process.

Fig. 4k presents the Jablonski diagram illustrating the possible photophysical processes involved in the PL. **2** is excited by 340 nm in CH_3OH, leading to the transition from the ground state of E to the singlet state of K in the excited state ($^1E^* \rightarrow {}^1K^*$). Over time, this state evolves into a keto-triplet state ($^1K^* \rightarrow {}^3K^*$) through ISC. When the temperature decreases from 300 K to 180 K, the ketone singlet lifetime increases from 160 ps to 2462 ps, resulting in reduced ISC efficiency and enhanced fluorescence emission at 545 nm. When excited by 400 nm light, **2** does not possess sufficient energy to overcome the energy barrier required for the transition from the enol-form to the keto-form.[57] Instead, **2** can transition from a locally excited state (LES) to a charge-separated state (CSS). The system ultimately relaxes to the ground state through a PCET process.[58,59] A detailed description of this mechanism and the corresponding TA spectral fitting are presented in Fig. S22.† However, as the temperature decreases, the radiative transition efficiency of this process is significantly reduced. At 180 K, the radiative efficiency becomes substantially lower than the non-radiative efficiency.

Construction of the Ex-De PL film and the anticounterfeiting application

2 displays remarkable Ex-De luminescence behavior at 250 K in CH_3OH. However, the low temperature and liquid environment limit its broader applications. To address this issue, we selected poly(vinyl alcohol) (PVA) as a polymeric matrix due to its abundant hydroxyl groups, which create a proton environment for **2** similar to that of CH_3OH.[60,61] Initially, 5 mg of **2** was added into a 10 mL PVA solution (5.0 wt%). After thorough mixing, the homogeneous mixture was poured into a round plastic dish and allowed to dry at 60 °C for 6 h in an oven.[62] Excitingly, the resulting **2**-PVA composite film not only retained the Ex-De PL properties but also functioned effectively at room temperature. As shown in the upper panel of Fig. 5a, when the film was excited with 344 nm light, two PL peaks at 442 and 534 nm were observed, with the latter being the primary peak. In contrast,
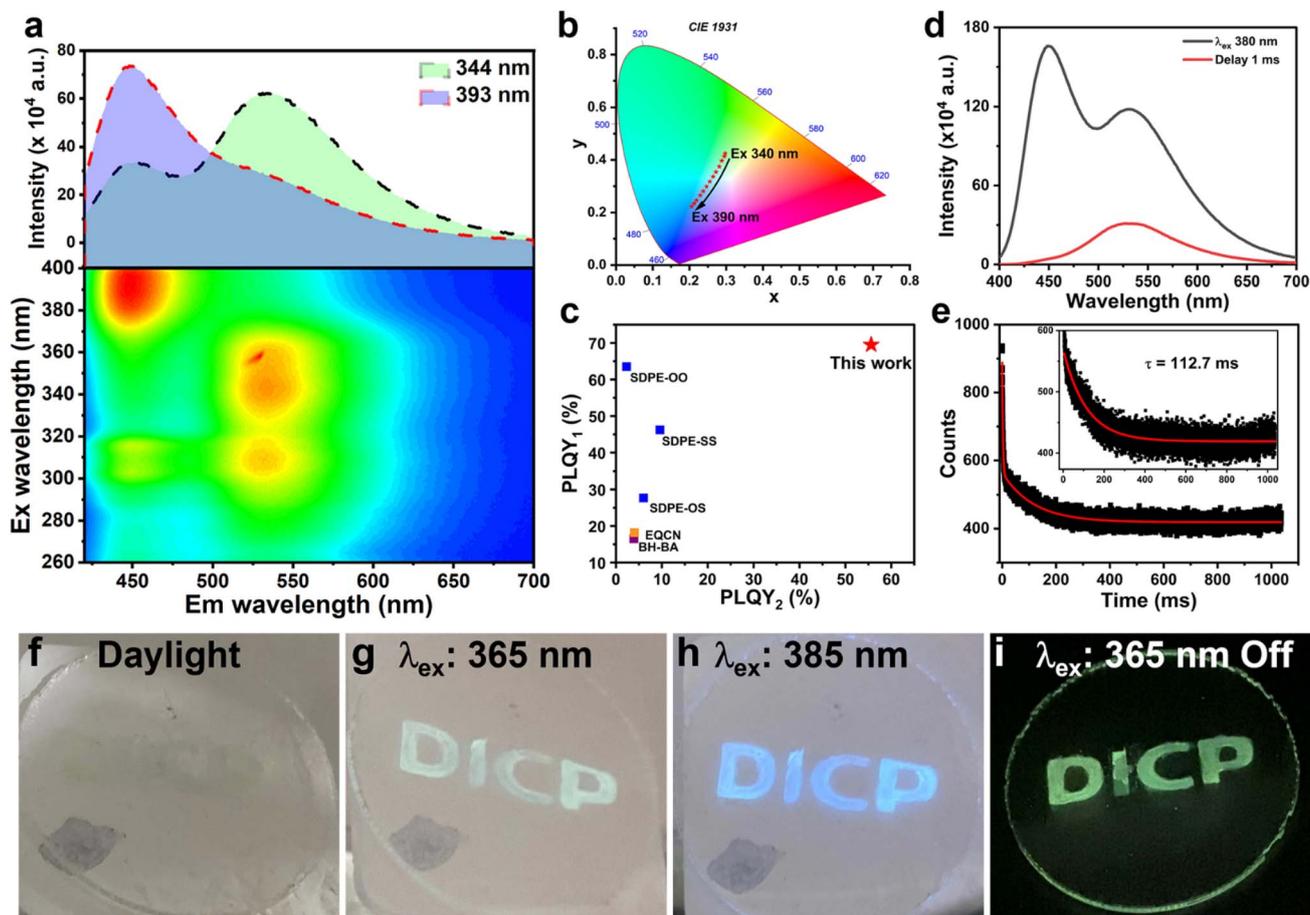

Fig. 5 PL properties of the **2** doped PVA film. (a) Excitation-emission mapping of the **2**-PVA film at room temperature. (b) CIE chromaticity diagram of the **2**-PVA film with λ_{ex} in the range of 340 to 390 nm. (c) Comparison of PLQY values for dual-luminescent centers in the **2**-PVA film (λ_{ex} at 363 nm and 396 nm), with other luminescent materials. (d) Fluorescence (black) and phosphorescence (red) emission spectra of the **2**-PVA film at room temperature, λ_{ex}: 380 nm. (e) A time-resolved phosphorescence decay curve of the **2**-PVA film at 545 nm, the red line is a fitting curve. (f–i) Printing the DICP pattern on an acrylic board, along with multimodal optical conversion, including films under ambient light (f), 365 nm UV illumination (g), 385 nm UV illumination (h), and after removal of 365 nm UV illumination (i), displaying the potential anti-counterfeiting application.

excitation at 393 nm resulted in a PL peak at 442 nm. The 2D contour map in the lower panel of Fig. 5a further illustrates this behavior. The PL peak at 534 nm could be excited by light in the range of 330 to 365 nm. As λ_{ex} increased from 370 nm to 410 nm, a strong emission peak emerged at 442 nm. When the film was excited by light at different wavelengths, a noticeable change in PL color from yellowish-green ((x, y) = 0.30, 0.42)) to blue ((x, y) = 0.21, 0.22)) was observed, as illustrated in the CIE coordinate diagram (Fig. 5b).

In addition, we measured the absolute PLQY of the **2**-PVA film using the Edinburgh Instrument FLS 980-STM. With the λ_{ex} set to 396 nm, the PLQY of the composite film was determined to be 55.6%, which increased to 69.6% after being irradiated at 363 nm. This phenomenon differed from the previously reported dual-wavelength center Ex-De PL systems, which typically exhibit a high PLQY at one λ_{ex} and a low value at the other λ_{ex}, as illustrated in Fig. 5c. The high PLQY values of the **2**-PVA composite film, under both λ_{ex}, are significantly higher than those reported in the literature, underscoring their potential for practical applications in Ex-De luminescent materials.[18,27,63] Furthermore, the composite film offered an additional advantage: delayed luminescence at room temperature (Fig. 5d). When the film was excited at λ_{ex} of 380 nm, the PL spectrum displayed two peaks at 447 nm and 534 nm. After a 1 ms delay following excitation, the emission spectrum revealed only one peak at 534 nm (red line of Fig. 5d). The phosphorescence decay time was measured using a triggered-accumulation multi-channel scaler (MCS) mode within the time-correlated single photon counting (TCSPC) system (SPC-150, Becker & Hickl GmbH, Germany). Fitting the data reveals a single-exponential decay with a lifetime τ of 112.7 ms (Fig. 5e). Based on the excellent performance of the composite film, we present a preliminary application in anti-counterfeiting. The **2**-PVA solution was poured into a mould featuring the lettering "DICP" on a transparent acrylic plate, representing the Dalian Institute of Chemical Physics. After drying for 6 h, a transparent and colorless film was obtained (Fig. 5f). Upon excitation with a 365 nm LED light, the clear "DICP" logo became visibly yellow-green (Fig. 5g). When excited with a 385 nm LED light, the logo's color changed to sky blue (Fig. 5h). These bright colors are easily discernible to the naked eye indoors under natural light. Moreover, in a dark room environment, excitation with the 365 nm LDE light followed by turning off the light source revealed a delayed green luminescence, which endowed the system with a third layer of information for encryption (Fig. 5i). Due to its plentiful color changes modulated by λ_{ex}, delayed luminescence at room temperature, and bright colors, the **2**-PVA composite system holds promise as an efficient, safe, and convenient anticounterfeiting material.

Conclusions

In summary, we introduced spinacine into an ESIPT molecule (**1**) to achieve Ex-De luminescence. Unlike **1**, the luminescence of **2** primarily occurs in the visible light region when dissolved in CH_3OH, with its luminescence color regulated by both temperature and λ_{ex}. Using molecule **2** as a model, while

preserving the structure of the single-HBT-based luminophore and the imidazole group, we designed compounds **3–6**, all of which exhibited remarkable Ex-De PL characteristics (Fig. S23 and Table S4†). We propose that the nitrogen-rich ligands such as spinacine, imidazole, and indole facilitate the electron transfer processes in the excited states of other monochromatic groups, which will motivate the discovery of more Ex-De molecules and expand our horizons regarding these interesting PL properties.

A detailed study of the mechanism reveals that the introduction of spinacine promotes the ESIPT process and stabilizes the keto-form excited state in CH_3OH. Besides, a novel progression known as PCET was introduced. It is unusual for a ligand to beneficially assist both processes, leading to significant Ex-De luminescence behavior. However, attributing these excited intermediates is complex and may be influenced by multiple factors (Fig. S24 and S25†). For instance, temperature can affect molecular configuration (Fig. S24†), which adds complexity to the mechanism analysis. The presence of multiple configurations and the potential influence of solvation effects may lead to various transition state species, complicating the attribution of different components.[64] Therefore, the mechanism discussed here is a preliminary finding warranting further investigation to uncover additional interesting effects or driving forces.

Given the limitations of Kasha's rule, a limited number of Ex-De PL materials exist in the domain of monochromatic organic light-emitting molecules. Further molecular designs and discoveries are essential to advance this field. We successfully incorporated **2** with PVA to create a composite film that exhibits robust Ex-De PL at room temperature. Notably, this **2**-PVA film demonstrates high quantum yields under both excitation conditions, which significantly enhances confidence in the practical application of Ex-De PL materials. However, a key challenge remains: improving the PLQY and achieving a broader range of luminescence colors in Ex-De PL materials based on single-chromophore organic molecules.[65] Additionally, existing Ex-De PL molecules generally exhibit poor solubility in aqueous solutions, posing a significant challenge for biosensing applications. We are committed to modifying the structure of **2** to enhance the hydrophilicity of these molecules, which is expected to pave the way in the field of ratiometric biosensing and multicolor imaging.[66]

Data availability

The data supporting this article have been included as part of the ESI.†

Author contributions

M. S. and M. L. contributed equally. M. S. and G. Q. conceived the project idea and wrote the manuscript. M. S., designed and synthesized molecules. M. S., M. L. G. Z. X. Y. and J. W. performed fs-TA and analyzed the results and contributed to the discussion of the manuscript. X. Z. and J. Z. performed ns-TA and UV-vis spectroelectrochemistry characterizations, and

DFT calculations, and contributed to the discussion of the manuscript. H. Q. performed NMR characterization. J. W. and Q. P. performed DFT calculations. M. S. and J. S. performed characterization of steady-state PL spectra. Z. Z. performed *in situ* FT-IR and analyzed the results, and Y. C., Y. Z. and D. W contributed to the discussion of the manuscript. All the authors discussed the results and implications and commented on the final manuscript.

Conflicts of interest

There are no conflicts to declare.

Acknowledgements

References

1 J. C. Del Valle and J. Catalan, *Phys. Chem. Chem. Phys.*, 2019, **21**, 10061–10069.

2 A. P. Demchenko, V. I. Tomin and P. T. Chou, *Chem. Rev.*, 2017, **117**, 13353–13381.

3 L. Shi, C. Yan, Z. Guo, W. Chi, J. Wei, W. Liu, X. Liu, H. Tian and W. H. Zhu, *Nat. Commun.*, 2020, **11**, 793.

4 G. Yang, Z. Liu, R. Zhang, X. Tian, J. Chen, G. Han, B. Liu, X. Han, Y. Fu, Z. Hu and Z. Zhang, *Angew. Chem., Int. Ed.*, 2020, **59**, 16154–16160.

5 L. Pan, S. Sun, A. Zhang, K. Jiang, L. Zhang, C. Dong, Q. Huang, A. Wu and H. Lin, *Adv. Mater.*, 2015, **27**, 7782–7787.

6 D. Li, J. Yang, M. Fang, B. Z. Tang and Z. Li, *Sci. Adv.*, 2022, **8**, eabl8392.

7 M. Du, Y. Shi, Q. Zhou, Z. Yin, L. Chen, Y. Shu, G. Y. Sun, G. Zhang, Q. Peng and D. Zhang, *Adv. Sci.*, 2022, **9**, e2104539.

8 D. Li, W. Hu, J. Wang, Q. Zhang, X. M. Cao, X. Ma and H. Tian, *Chem. Sci.*, 2018, **9**, 5709–5715.

9 J. Wang, Y. Yang, K. Li, L. Zhang and Z. Li, *Angew. Chem., Int. Ed.*, 2023, **62**, e202304020.

10 J. Chen, X. Chen, Y. Liu, Y. Li, J. Zhao, Z. Yang, Y. Zhang and Z. Chi, *Chem. Sci.*, 2021, **12**, 9201–9206.

11 Y. K. Jeong, Y. M. Lee, J. Yun, T. Mazur, M. Kim, Y. J. Kim, M. Dygas, S. H. Choi, K. S. Kim, O. H. Kwon, S. M. Yoon and B. A. Grzybowski, *J. Am. Chem. Soc.*, 2017, **139**, 15088–15093.

12 Q. Fu, J. Zhang, K. Zhang, S. Sun and Z. Dong, *J. Mater. Chem. A*, 2025, **13**, 36–72.

13 Y. J. Ma, F. Xu, X. Y. Ren, F. Y. Chen, J. Pan, J. H. Li, S. D. Han and G. M. Wang, *Chem. Sci.*, 2024, **15**, 17642–17651.

14 J. G. Yang, K. Li, J. Wang, S. Sun, W. Chi, C. Wang, X. Chang, C. Zou, W. P. To, M. D. Li, X. Liu, W. Lu, H. X. Zhang,

15 C. M. Che and Y. Chen, *Angew. Chem., Int. Ed.*, 2020, **59**, 6915–6922.

16 J. Li, K. Chen, J. Wei, Y. Ma, R. Zhou, S. Liu, Q. Zhao and W. Y. Wong, *J. Am. Chem. Soc.*, 2021, **143**, 18317–18324.

17 L. C. Lee and K. K. Lo, *J. Am. Chem. Soc.*, 2022, **144**, 14420–14440.

18 Z. Liu, W. He and Z. Guo, *Chem. Soc. Rev.*, 2013, **42**, 1568–1600.

19 Z. Man, Z. Lv, Z. Xu, M. Liu, J. He, Q. Liao, J. Yao, Q. Peng and H. Fu, *J. Am. Chem. Soc.*, 2022, **144**, 12652–12660.

20 Q. Zhou, T. Yang, Z. Zhong, F. Kausar, Z. Wang, Y. Zhang and W. Z. Yuan, *Chem. Sci.*, 2020, **11**, 2926–2933.

21 H. Wang, Q. Li, P. Alam, H. Bai, V. Bhalla, M. R. Bryce, M. Cao, C. Chen, S. Chen, X. Chen, Y. Chen, Z. Chen, D. Dang, D. Ding, S. Ding, Y. Duo, M. Gao, W. He, X. He, X. Hong, Y. Hong, J. J. Hu, R. Hu, X. Huang, T. D. James, X. Jiang, G. I. Konishi, R. T. K. Kwok, J. W. Y. Lam, C. Li, H. Li, K. Li, N. Li, W. J. Li, Y. Li, X. J. Liang, Y. Liang, B. Liu, G. Liu, X. Liu, X. Lou, X. Y. Lou, L. Luo, P. R. McGonigal, Z. W. Mao, G. Niu, T. C. Owyong, A. Pucci, J. Qian, A. Qin, Z. Qiu, A. L. Rogach, B. Situ, K. Tanaka, Y. Tang, B. Wang, D. Wang, J. Wang, W. Wang, W. X. Wang, W. J. Wang, X. Wang, Y. F. Wang, S. Wu, Y. Wu, Y. Xiong, R. Xu, C. Yan, S. Yan, H. B. Yang, L. L. Yang, M. Yang, Y. W. Yang, J. Yoon, S. Q. Zang, J. Zhang, P. Zhang, T. Zhang, X. Zhang, X. Zhang, N. Zhao, Z. Zhao, J. Zheng, L. Zheng, Z. Zheng, M. Q. Zhu, W. H. Zhu, H. Zou and B. Z. Tang, *ACS Nano*, 2023, **17**, 14347–14405.

22 K. Wu, T. Zhang, Z. Wang, L. Wang, L. Zhan, S. Gong, C. Zhong, Z. H. Lu, S. Zhang and C. Yang, *J. Am. Chem. Soc.*, 2018, **140**, 8877–8886.

23 X. Tian, L. C. Murfin, L. Wu, S. E. Lewis and T. D. James, *Chem. Sci.*, 2021, **12**, 3406–3426.

24 Y. Su, Y. Zhang, Z. Wang, W. Gao, P. Jia, D. Zhang, C. Yang, Y. Li and Y. Zhao, *Angew. Chem., Int. Ed.*, 2020, **59**, 9967–9971.

25 X. Dou, T. Zhu, Z. Wang, W. Sun, Y. Lai, K. Sui, Y. Tan, Y. Zhang and W. Z. Yuan, *Adv. Mater.*, 2020, **32**, e2004768.

26 H. Li, J. Gu, Z. Wang, J. Wang, F. He, P. Li, Y. Tao, H. Li, G. Xie, W. Huang, C. Zheng and R. Chen, *Nat. Commun.*, 2022, **13**, 429.

27 P. She, J. Duan, J. Lu, F. Qin, F. Li, C. Liu, S. Liu, Y. Ma and Q. Zhao, *Adv. Opt. Mater.*, 2022, **10**, 2102706.

28 Y. H. Wu, H. Xiao, B. Chen, R. G. Weiss, Y. Z. Chen, C. H. Tung and L. Z. Wu, *Angew. Chem., Int. Ed.*, 2020, **59**, 10173–10178.

29 X. Zhang, C. Chen, W. Zhang, N. Yin, B. Yuan, G. Zhuang, X. Y. Wang and P. Du, *Nat. Commun.*, 2024, **15**, 2684.

30 Y. Shen, Z. An, H. Liu, B. Yang and Y. Zhang, *Angew. Chem., Int. Ed.*, 2023, **62**, e202214483.

31 W. Zhao, Z. He and B. Z. Tang, *Nat. Rev. Mater.*, 2020, **5**, 869–885.

32 W. Li, Y. Han, L. Wang, G. S. Selopal, X. Wang and H. Zhao, *RSC Adv.*, 2024, **14**, 83–89.

33 A. Shukla, V. T. N. Mai, V. V. Divya, C. H. Suresh, M. Paul, V. Karunakaran, S. K. M. McGregor, I. Allison,

K. N. Narayanan Unni, A. Ajayaghosh, E. B. Namdas and S. C. Lo, *J. Am. Chem. Soc.*, 2022, **144**, 13499–13510.

33 H. Hu, X. Cheng, Z. Ma, R. P. Sijbesma and Z. Ma, *J. Am. Chem. Soc.*, 2022, **144**, 9971–9979.

34 A. C. Sedgwick, L. Wu, H. H. Han, S. D. Bull, X. P. He, T. D. James, J. L. Sessler, B. Z. Tang, H. Tian and J. Yoon, *Chem. Soc. Rev.*, 2018, **47**, 8842–8880.

35 S. Zuo, Y. Wang, J. Wan, Y. Ma and Z. Yan, *Small*, 2024, **20**, e2307102.

36 N. Inada, N. Fukuda, T. Hayashi and S. Uchiyama, *Nat. Protoc.*, 2019, **14**, 1293–1321.

37 P. Y. Fu, B. N. Li, Q. S. Zhang, J. T. Mo, S. C. Wang, M. Pan and C. Y. Su, *J. Am. Chem. Soc.*, 2022, **144**, 2726–2734.

38 Y. Sun, M. Fu, M. Bian and Q. Zhu, *Biotechnol. Bioeng.*, 2023, **120**, 7–21.

39 M. Liu, P. Xia, G. Zhao, C. Nie, K. Gao, S. He, L. Wang and K. Wu, *Angew. Chem., Int. Ed.*, 2022, **61**, e202208241.

40 H. W. Tseng, J. Q. Liu, Y. A. Chen, C. M. Chao, K. M. Liu, C. L. Chen, T. C. Lin, C. H. Hung, Y. L. Chou, T. C. Lin, T. L. Wang and P. T. Chou, *J. Phys. Chem. Lett.*, 2015, **6**, 1477–1486.

41 M. Barbatti, A. J. Aquino, H. Lischka, C. Schriever, S. Lochbrunner and E. Riedle, *Phys. Chem. Chem. Phys.*, 2009, **11**, 1406–1415.

42 S. M. Aly, A. Usman, M. AlZayer, G. A. Hamdi, E. Alarousu and O. F. Mohammed, *J. Phys. Chem. B*, 2015, **119**, 2596–2603.

43 V. S. Padalkar and S. Seki, *Chem. Soc. Rev.*, 2016, **45**, 169–202.

44 K. Sakai, S. Takahashi, A. Kobayashi, T. Akutagawa, T. Nakamura, M. Dosen, M. Kato and U. Nagashima, *Dalton Trans.*, 2010, **39**, 1989–1995.

45 T. Elsaesser and B. Schmetzer, *Chem. Phys. Lett.*, 1987, **140**, 293–299.

46 J. E. Kwon and S. Y. Park, *Adv. Mater.*, 2011, **23**, 3615–3642.

47 E. Odella, S. J. Mora, B. L. Wadsworth, M. T. Huynh, J. J. Goings, P. A. Liddell, T. L. Groy, M. Gervaldo, L. E. Sereno, D. Gust, T. A. Moore, G. F. Moore, S. Hammes-Schiffer and A. L. Moore, *J. Am. Chem. Soc.*, 2018, **140**, 15450–15460.

48 G. A. Parada, Z. K. Goldsmith, S. Kolmar, B. Pettersson Rimgard, B. Q. Mercado, L. Hammarström, S. Hammes-Schiffer and J. M. Mayer, *Science*, 2019, **364**, 471–475.

49 S. J. Mora, E. Odella, G. F. Moore, D. Gust, T. A. Moore and A. L. Moore, *Acc. Chem. Res.*, 2018, **51**, 445–453.

50 X. Chen, X. Zhang, X. Xiao, Z. Wang and J. Zhao, *Angew. Chem., Int. Ed.*, 2023, **62**, e202216010.

51 X. Xiao, Y. Yan, A. A. Sukhanov, S. Doria, A. Iagatti, L. Bussotti, J. Zhao, M. Di Donato and V. K. Voronkova, *J. Phys. Chem. B*, 2023, **127**, 6982–6998.

52 T. Lu and F. Chen, *J. Comput. Chem.*, 2012, **33**, 580–592.

53 T. Lu, *J. Chem. Phys.*, 2024, **161**, 082503.

54 Y. Wu, Z. Zhao and Z. Peng, *ACS Energy Lett.*, 2023, **8**, 3430–3436.

55 Y. Yoneda, S. J. Mora, J. Shee, B. L. Wadsworth, E. A. Arsenault, D. Hait, G. Kodis, D. Gust, G. F. Moore, A. L. Moore, M. Head-Gordon, T. A. Moore and G. R. Fleming, *J. Am. Chem. Soc.*, 2021, **143**, 3104–3112.

56 R. Tyburski, T. Liu, S. D. Glover and L. Hammarstrom, *J. Am. Chem. Soc.*, 2021, **143**, 560–576.

57 N. Sülzner, G. Jung and P. Nuernberger, *Chem. Sci.*, 2025, **16**, 1560–1596.

58 S. K. Thiyagarajan, R. Suresh, V. Ramanan and P. Ramamurthy, *Chem. Sci.*, 2018, **9**, 910–921.

59 L. Biczók, N. Gupta and H. Linschitz, *J. Am. Chem. Soc.*, 1997, **119**, 12601–12609.

60 D. Li, Y. Yang, J. Yang, M. Fang, B. Z. Tang and Z. Li, *Nat. Commun.*, 2022, **13**, 347.

61 X. Zhang, Y. Cheng, J. You, J. Zhang, C. Yin and J. Zhang, *Nat. Commun.*, 2022, **13**, 1117.

62 F. Zhang, Q. Li, C. Wang, D. Wang, M. Song, Z. Li, X. Xue, G. Zhang and G. Qing, *Adv. Funct. Mater.*, 2022, **32**, 2204487.

63 Y. Zhang, H. Yang, H. Ma, G. Bian, Q. Zang, J. Sun, C. Zhang, Z. An and W. Y. Wong, *Angew. Chem., Int. Ed.*, 2019, **58**, 8773–8778.

64 D. Ushakou and M. Jozefowicz, *Phys. Chem. Chem. Phys.*, 2024, **26**, 25029–25047.

65 W. L. Zhou, X. Y. Dai, W. Lin, Y. Chen and Y. Liu, *Chem. Sci.*, 2023, **14**, 6457–6466.

66 J. Zhang, X. Chai, X. P. He, H. J. Kim, J. Yoon and H. Tian, *Chem. Soc. Rev.*, 2019, **48**, 683–722.